

1 **Understanding the processes that control the interannual variability of the Northern**
2 **Hemisphere wintertime polar front and subtropical jet streams**

3 **Xinhuiyu Liu¹, Kevin M. Grise¹, Daniel F. Schmidt¹, Robert E. Davis¹**

4

5 ¹ Department of Environmental Sciences, University of Virginia, Charlottesville, VA, USA

6

7 Corresponding author: Xinhuiyu Liu (xl7pd@virginia.edu)

8

9 **Key Points:**

- 10 • The interannual movement and intensification of the Northern Hemisphere wintertime
11 polar front jet reflect variations in surface baroclinicity.
- 12 • Variations in tropical convection over the Pacific Ocean are linked to variations of the
13 Northern Hemisphere wintertime subtropical jet.
- 14 • Tropical convection in CMIP6 models is often displaced westward when compared to
15 observations, reflecting a climatological bias.

16 **Abstract**

17 The interannual movement and intensification of the subtropical jet (STJ) and polar front
18 jet (PFJ) streams have important implications for global and regional climate. Previous studies
19 have related the position and strength of the STJ to tropical thermodynamic processes, whereas
20 the position and strength of the PFJ are more associated with mid-latitude eddies. These
21 conclusions have largely resulted from studies using idealized models. In this study, ERA-
22 Interim reanalysis and CMIP6 global climate models are used to examine the mechanisms
23 responsible for controlling the interannual variability of the STJ and PFJ at different longitudes
24 in the Northern Hemisphere (NH) during winter. Consistent with idealized modeling studies, a
25 close relationship is found between tropical outgoing longwave radiation (OLR) and the STJ, and
26 between mid-latitude surface temperature gradients and the PFJ. The movement and
27 intensification of the NH PFJ reflect variations in surface baroclinicity. Variations in tropical
28 convection over the Pacific Ocean are linked to variations in the strength and position of the NH
29 STJ at almost all longitudes, with different phases of the El Niño-Southern Oscillation (ENSO)
30 associated with the poleward shift and strengthening of the STJ in different regions. CMIP6
31 models generally capture these relationships, but the models' tropical convection is often
32 displaced westward when compared to observations, reflecting a climatological bias in OLR in
33 the western tropical Pacific Ocean in many models. The displaced tropical convection in models
34 excites different paths of Rossby wave propagation, resulting in different ENSO teleconnections
35 on the STJ over North America and Europe.

36

37 **1. Introduction**

38 Jet streams are relatively narrow bands of strong west-to-east winds in the upper
39 troposphere. In the zonal mean climatology, there are two jet streams, the subtropical jet (STJ)
40 and polar front jet (PFJ), located in both the Northern Hemisphere (NH) and Southern
41 Hemisphere (SH). The STJ is commonly viewed as being driven by the angular momentum
42 conservation in the poleward flowing upper tropospheric branch of the tropical Hadley
43 circulation (Held & Hou, 1980; Schneider, 1977), and thus it is located near the poleward edge
44 of Hadley Cell in each hemisphere. The PFJ is driven by the convergence of momentum by
45 transient midlatitude eddies (Held, 1975; Panetta, 1993) and is consequently located at mid-
46 latitudes where baroclinic instability is strongest.

47 This simple picture of the two jet streams, however, does not apply at all longitudes and
48 in all seasons. For example, in the NH wintertime climatology, there are clearly two distinct jets
49 in Eurasia, the Eastern Pacific Ocean, and the North Atlantic Ocean, while the STJ and PFJ are
50 merged into a single jet stream in East Asia, the Western Pacific Ocean, and the Eastern United
51 States (Christenson, Martin, & Handlos, 2017; Eichelberger & Hartmann, 2007; Koch, Wernli, &
52 Davies, 2006; Li & Wettstein, 2012). The strength of the two jets also varies by region, with both
53 the STJ and PFJ usually strongest over the Pacific Ocean during winter (Archer & Caldeira,
54 2008; Koch et al., 2006). The NH jet streams are weaker and further poleward during summer
55 months (Archer and Caldeira 2008; Koch et al. 2006; Woollings et al. 2014). In the Southern
56 Hemisphere (SH), a single jet stream is observed during summer, whereas somewhat more
57 distinct subtropical and polar front jets are observed during winter (Bals-Elsholz et al., 2001;
58 Kim & Lee, 2004)

59 The positions and strengths of the jets are not constant in time and vary from month to
60 month and from year to year. Understanding variability in the position and strength of the jet
61 streams is important, as it directly influences impactful surface weather events, such as
62 extratropical cyclone tracks (Dickson and Namias 1976; Athanasiadis et al. 2010), blocking
63 anticyclone frequency (Kaas and Branstator 1993; Barnes and Hartmann 2010; Woollings et al.
64 2018), heatwaves and cold air outbreaks (Mahlstein, Martius, Chevalier, & Ginsbourger, 2012;
65 Petoukhov, Rahmstorf, Petri, & Schellnhuber, 2013), and atmospheric rivers and their associated
66 heavy precipitation events (Ryoo et al., 2013; Zhang & Villarini, 2018). Previous studies have
67 documented relationships between variability in the jet streams and known teleconnection
68 patterns, including but not limited to the El Niño-Southern Oscillation (ENSO), the Northern
69 Annular Mode (NAM)/North Atlantic Oscillation (NAO), the Pacific-North American
70 teleconnection pattern (PNA), and the Southern Annular Mode (SAM). Variability in the PFJ is
71 closely tied to the NAM/NAO, PNA, and SAM (Gallego, Ribera, Garcia-Herrera, Hernandez, &
72 Gimeno, 2005; Strong & Davis, 2008; Woollings et al., 2014), whereas variability in the STJ is
73 expected to correlate with ENSO (Gallego et al., 2005; Lu, Chen, & Frierson, 2008; Seager et al.,
74 2003). Jet streams, of course, also vary with synoptic weather systems on daily timescales
75 (Handlos & Martin, 2016; Winters & Martin, 2016), but in this study, we focus on month-to-
76 month and interannual variability of the two jet streams.

77 Whether the STJ and PFJ are merged together or in two distinct branches may also have
78 important implications for global and regional climate. One example is the relative minimum in
79 North Pacific storm track activity that occurs during mid-winter (January and February), even
80 though the baroclinicity is the strongest during these months (Nakamura, 1992). A similar
81 feature occurs in the North Atlantic storm track during years with a strong STJ (Afargan &

82 Kaspi, 2017). Several recent studies have attributed the existence of a mid-winter storm track
83 minimum to the merging of the STJ and PFJ (Yuval et al. 2018; Novak et al. 2020). Previous
84 studies have used idealized models to explain the merging and splitting of the two jets. Lee and
85 Kim (2003) found that, when the STJ is relatively weak, the most favorable region for baroclinic
86 wave growth often lies in midlatitudes, establishing an eddy-driven PFJ that is well separated
87 from the STJ. In contrast, when the STJ is relatively strong, baroclinic wave growth occurs close
88 enough to the STJ so that a single merged jet evolves. Son and Lee (2005) further found that a
89 single merged jet forms preferentially when tropical heating is strong, while a double-jet state
90 forms when tropical heating is weak enough to allow midlatitude eddies to grow more poleward
91 and form a separate eddy-driven jet. Yuval and Kaspi (2018) concluded that baroclinic eddies are
92 stronger when there is a strong distinct PFJ and are weaker when there is a merged jet.

93 These idealized model results provide insight into the processes that control the
94 variability of the polar front and subtropical jets, but they are not entirely consistent with the jet
95 characteristics found in observations or comprehensive global climate models. Based on the
96 results of Lee and Kim (2003), one might expect that the positions and strengths of the STJ and
97 PFJ are negatively correlated. That is, when the STJ is weak and equatorward, there should be a
98 strong and poleward PFJ. However, several recent studies have found that interannual variability
99 in the position and strength of the jets is only weakly correlated in the zonal mean (Davis &
100 Birner, 2016, 2017; Menzel et al., 2019; Solomon et al., 2016; Waugh et al., 2018). To our
101 knowledge, the relationship between the interannual variability in the position and strength of the
102 jets has not been examined in detail at individual longitudes.

103 The purpose of this study is to better understand the interannual variability in the position
104 and strength of the STJ and PFJ at individual longitudes. To do this, we define the position and

105 strength of polar front and subtropical jets using both reanalysis data and global climate models.
106 For this study, we focus our analysis on the wintertime (December–February) jets in the NH
107 because longitudinal asymmetries are much greater in the NH and the jets are strongest in the
108 winter season when the pole-to-equator temperature gradient is largest. We find that variations
109 in (1) tropical convective heating and (2) horizontal surface temperature gradients at midlatitudes
110 are closely linked to interannual variations in the position and intensity of the jet streams.
111 Tropical convective heating plays a more important role in modulating the STJ, consistent with
112 the idealized modeling studies discussed above (Lee & Kim, 2003; Son & Lee, 2005),
113 observations associated with the El Niño-Southern Oscillation (Gallego et al., 2005; Lu et al.,
114 2008), and case studies of synoptic-scale weather events (Handlos & Martin, 2016; Winters &
115 Martin, 2016). Horizontal surface temperature gradients are critical in modulating the PFJ, as
116 variations in baroclinicity are closely linked to the location and strength of the PFJ (Brayshaw et
117 al. 2008; Sampe et al. 2010; Hall et al. 2015).

118 The paper is organized as follows. Section 2 describes the data and methods used in this
119 study. Section 3 examines the interannual variability in STJ and PFJ position and strength in
120 observations, and their linkage to tropical convective heating and midlatitude horizontal surface
121 temperature gradients. Section 4 explores the causes of model biases in these relationships.
122 Section 5 concludes with a discussion and summary of the results.

123

124 **2. Data and Methods**

125 2.1 Data

126

127 To examine observed variability in the jets, we use monthly-mean wintertime
128 (December–February) zonal wind and surface temperature data from the European Centre for
129 Medium-Range Weather Forecasts (ECMWF) Interim reanalysis data set (ERA-Interim; Dee et
130 al., 2011). The data are provided at a spatial resolution of 0.75 degrees latitude \times 0.75 degrees
131 longitude. We also make use of monthly-mean outgoing longwave radiation (OLR) data from the
132 National Oceanic and Atmospheric Administration (NOAA) interpolated OLR dataset
133 (Liebmann & Smith, 1996), which has a spatial resolution of 2.5 degrees latitude \times 2.5 degrees
134 longitude. Our observational analysis is based on the 40-year period from January 1979 to
135 December 2018.

136 To compare the observed jet variability with that in global climate models, we examine
137 output from the historical runs of 23 global climate models that participated in phase 6 of the
138 Coupled Model Intercomparison Project (CMIP6; Eyring et al., 2016), which are listed in Table
139 S1 in the supplementary material. The historical runs of the models are designed to simulate the
140 past climate over the period 1850–2014 by prescribing observed changes in radiative forcings
141 (greenhouse gases, stratospheric and tropospheric ozone, tropospheric aerosols, volcanic
142 eruptions, changes in solar output, etc.). We examine one ensemble member per model. The
143 spatial resolution of the model output is highly variable and ranges from about 0.7 degrees to
144 about 2.8 degrees (Table S1), so before analysis, all variables are interpolated to a common
145 spatial resolution of 2.5 degrees latitude \times 2.5 degrees longitude. All of the model analyses are
146 based on the 36-year period from 1979 to 2014, as the models' historical runs end in 2014. The

147 observational analysis based on the 40-year period from 1979 to 2018 is very similar to that
148 based on the 36-year period from 1979 to 2014 and thus can be directly compared to the model
149 analyses in this study.

150 2.2 Methods

151
152 To define the position and strength of the PFJ and STJ, we exploit the fact that the STJ is
153 defined by a baroclinic vertical structure (strong westerlies aloft and near-zero surface winds),
154 whereas the PFJ is defined by an equivalent barotropic vertical structure (westerly wind
155 maximum throughout the depth of the vertical column). Even though the wind speeds associated
156 with both jets are maximized in the upper troposphere, it is challenging to uniquely identify the
157 position and strength of each jet using the upper tropospheric wind field alone. Thus, following
158 previous studies, we define the position and strength of the PFJ using the lower tropospheric
159 wind field (e.g., Ceppi & Hartmann, 2013; Barnes & Polvani 2013). Specifically, in this study,
160 we define the position of the PFJ as the latitude of the maximum of the lower tropospheric (850
161 hPa) zonal wind averaged over a given longitude band between 20°N and 65°N. The location of
162 maximum winds is determined by fitting a quadratic to the peak and finding the latitude of
163 maximum wind speed at an interval of 0.01° (Barnes & Polvani, 2013). The strength of the PFJ
164 is then determined using the value of the 850 hPa zonal wind at the identified PFJ latitude.

165 We define the position of the STJ as the latitude of the maximum value found in the
166 difference field between the upper tropospheric (250 hPa) zonal wind and the lower tropospheric
167 (850 hPa) zonal wind averaged over a given longitude band between 10°N and 40°N. The lower
168 tropospheric zonal wind is subtracted to isolate the vertically integrated thermal wind shear
169 (Davis & Birner, 2016), as the STJ is defined by strong westerlies aloft and near-zero surface

170 winds. In the zonal mean, this method yields a comparable position to the NH subtropical jet
171 identified using tropopause height gradients (Maher et al., 2020). The strength of the STJ is then
172 determined using the value of the upper tropospheric (250 hPa) zonal wind at the identified STJ
173 latitude.

174 The above definitions of the jet streams have been used in a number of recent studies for
175 zonal-mean diagnostics (Adam et al. 2018; Waugh et al. 2018). However, here we intend to
176 apply these definitions both in the zonal mean and at specific longitudes. To do this, we define
177 regional jet indices, in which north-south zonal wind profiles are averaged over specific
178 longitude bands prior to finding the jet positions and strengths. The six regions are defined as:
179 Europe (0°-50°E), Asia (50°E-130°E), the Western Pacific Ocean (130°E-160°W), the Eastern
180 Pacific Ocean (160°W-130°W), North America (130°W-80°W), and the Atlantic Ocean (80°W-
181 0°). We also calculate the four jet indices (PFJ position, PFJ strength, STJ position, STJ
182 strength) at each individual longitude (i.e., using the north-south zonal wind profile at each
183 longitude) (see Fig. 1).

184

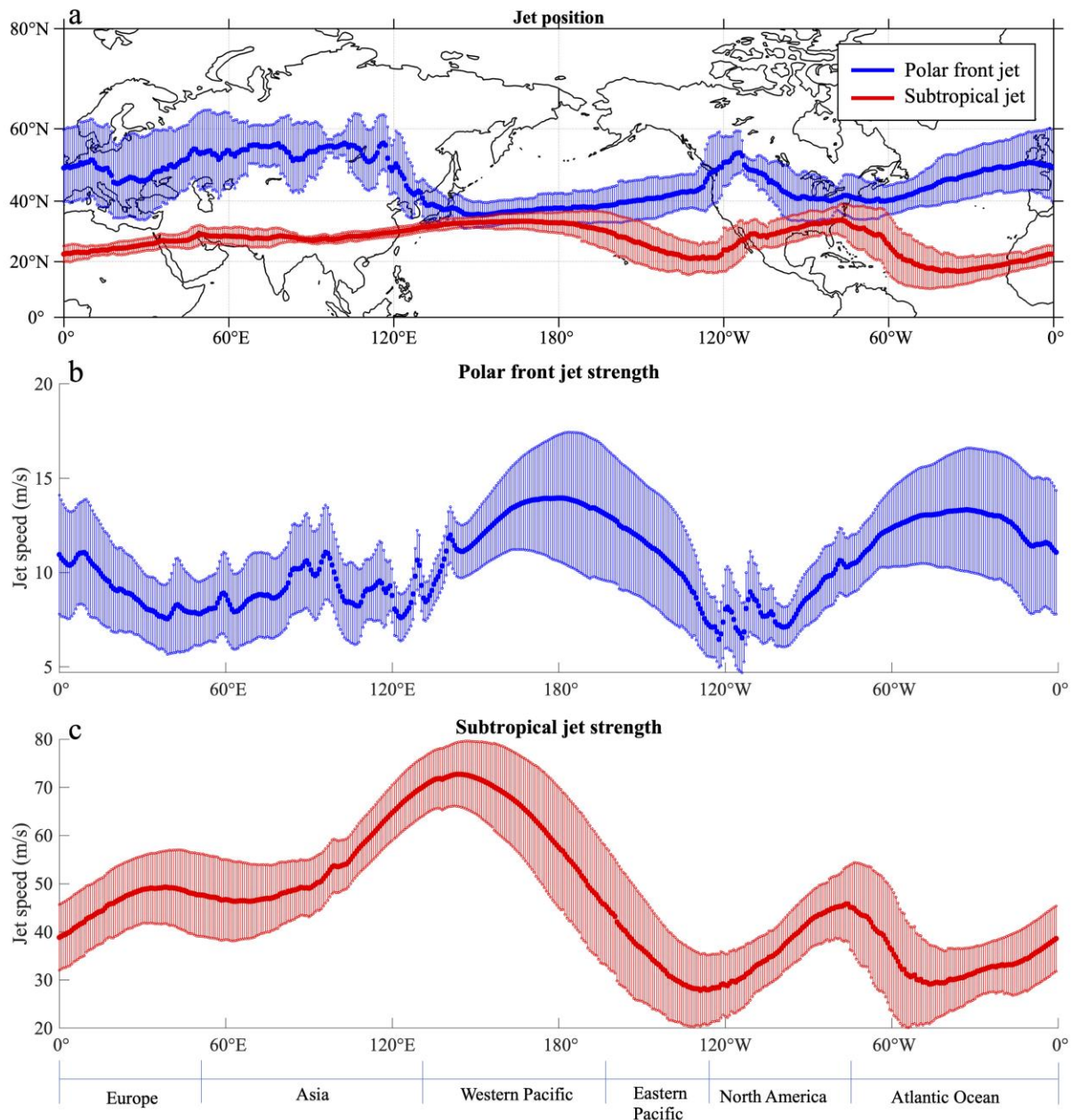
185 **3. Observed variability in the subtropical and polar front jet streams**

186 We begin by reviewing the observed climatology of the NH wintertime jet positions and
187 strengths. Figure 1 shows the NH wintertime (December–February) climatological positions
188 (Fig. 1a) and strengths (Fig. 1b and Fig. 1c) of the polar front and subtropical jets along with
189 their standard deviations at each longitude. In the NH wintertime climatology, there are clearly
190 two distinct jets in Eurasia, the Eastern Pacific Ocean, and the North Atlantic Ocean, while the
191 STJ and PFJ are merged into a single jet stream in East Asia, the Western Pacific Ocean, and the
192 Eastern United States (Fig. 1a), as also documented in previous studies (Christenson et al., 2017;

193 Eichelberger & Hartmann, 2007; Koch et al., 2006; Li & Wettstein, 2012). The PFJ position has
194 a similar standard deviation at most longitudes (6.73 degrees latitude on average), with the
195 largest standard deviations occurring over western Eurasia. In contrast, the standard deviation of
196 the STJ position varies more substantially by longitude, with very small standard deviations
197 (2.09 degrees latitude) over Eurasia and the western Pacific Ocean and standard deviations
198 comparable to that of the PFJ position at most other longitudes.

199 The strength of the two jets also varies by region. The strength of the PFJ (as measured
200 by the 850-hPa zonal wind maximum) is largest (10–15 m/s zonal wind at 850 hPa) and displays
201 the most variance over the storm track regions of the North Pacific and North Atlantic Oceans
202 (Fig. 1b). The strength of the STJ (as measured by the 250-hPa zonal wind maximum) is largest
203 (> 40 m/s zonal wind at 250 hPa) over Eurasia and the western Pacific Ocean, with the largest
204 wind speeds (~70 m/s) observed where the STJ and PFJ are merged over the western Pacific
205 Ocean (Fig. 1c). A secondary peak in STJ strength is also observed in eastern North America
206 where the two jets are merged. The standard deviation of the STJ strength varies little with
207 longitude.

Mean positions and strengths of the polar front and subtropical jet



208

209 **Figure 1.** Mean positions (a) and strengths (b and c) of NH wintertime (December–February)
 210 polar front and subtropical jet with ± 1 standard deviation (shading) shown at all longitudes using
 211 jet indices derived from the ERA-Interim reanalysis dataset from 1979–2018. Note that the jet
 212 speeds in panels b and c are plotted on different scales. The polar front jet is defined at 850 hPa
 213 whereas the subtropical jet is at 250 hPa.

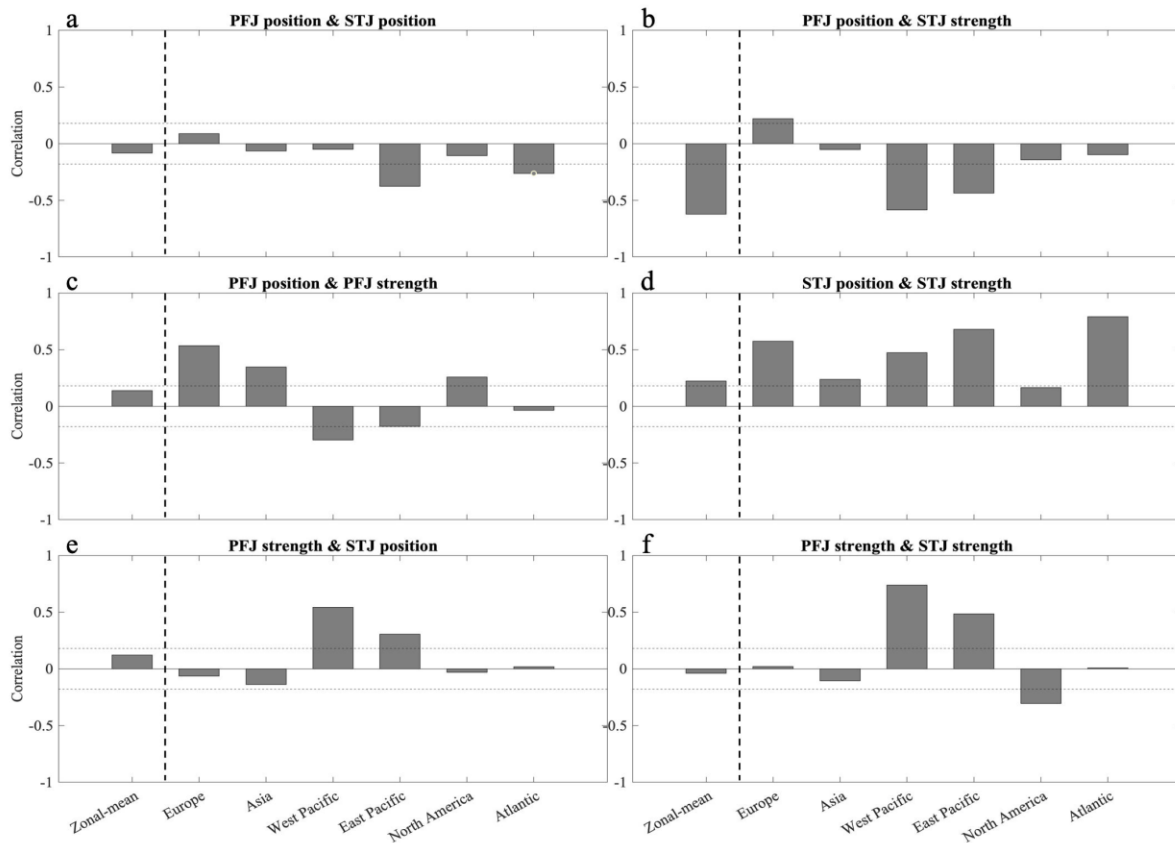
214 We next examine whether variability in the jet strengths and positions are correlated with
215 one another, as could be anticipated from the results of Lee and Kim (2003). Figure 2 shows the
216 correlations among the monthly time series of the positions and strengths of the STJ and PFJ.
217 The correlations are shown for the zonal-mean (leftmost bar in each panel) and the 6 different
218 regions defined in Section 2.2. The horizontal dashed lines in each panel indicate the minimum
219 value for statistically significant correlations at the 95% confidence level.

220 With respect to the overall correlations between position and strength from the zonal-
221 mean wind field, few statistically significant correlations are found, consistent with the results of
222 Menzel et al. (2019). A significant negative correlation is found between the PFJ position and
223 STJ strength (Fig. 2b), as a more poleward distinct PFJ is associated with a weaker STJ (as could
224 be anticipated from the results of Lee and Kim 2003). A weakly significant positive correlation
225 is also found between the strength and position of the STJ (Fig. 2d), in contrast to the weak
226 negative correlation found in climate models by Menzel et al. (2019). This difference could be
227 due to the fact that Menzel et al. (2019) defined STJ strength using the difference field between
228 the upper tropospheric (250 hPa) zonal wind and the lower tropospheric (850 hPa) zonal wind,
229 whereas in this study, we use only the upper tropospheric (250 hPa) zonal wind to define the STJ
230 strength. If we define the STJ strength as in Menzel et al. (2019), we also find a weak negative
231 correlation (-0.0718) between STJ position and strength.

232 However, the weak correlations among the positions and strengths of the jets in the zonal
233 mean mask significant correlations among the positions and strengths of the jets that occur on the
234 regional level, which highlights the need to examine the variability of the jets and the underlying
235 mechanisms at individual longitudes. As in the zonal mean (Davis & Birner 2017; Waugh et al.
236 2018; Menzel et al. 2019), there are few significant correlations between the positions of the PFJ

237 and STJ, except in the Eastern Pacific and Atlantic sectors where a small negative relationship is
 238 observed (Fig. 2a). Consistent with the results of Lee and Kim (2003), the PFJ position is
 239 negatively correlated with the STJ strength in the zonal mean, and this negative correlation arises
 240 predominantly from the Pacific Ocean regions (Fig. 2b). However, in other regions, the
 241 correlations are small. The strength and position of the PFJ are positively correlated over
 242 continents and negatively correlated over oceans (Fig. 2c), whereas the strength and position of
 243 the STJ are positively correlated in all regions (Fig. 2d). Significant positive correlations also
 244 exist between the PFJ strength and STJ position/strength over the Pacific Ocean, particularly in
 245 the Western Pacific where there is a merged jet (Fig. 2e and Fig. 2f).

Cross-correlations between four jet indices



246

247 **Figure 2.** Correlations between monthly time series of the positions and strengths of the
 248 subtropical and polar front jets during NH winter, based on ERA-Interim reanalysis (1979–

249 2018). The jets are defined in the zonal mean and for the six different regions defined in Section
250 2.2. The seasonal cycle is removed prior to the analysis. The horizontal dashed lines in each
251 panel indicate the minimum value for significant correlations at the 95% confidence level
252 according to a two-tailed Student's t-test.

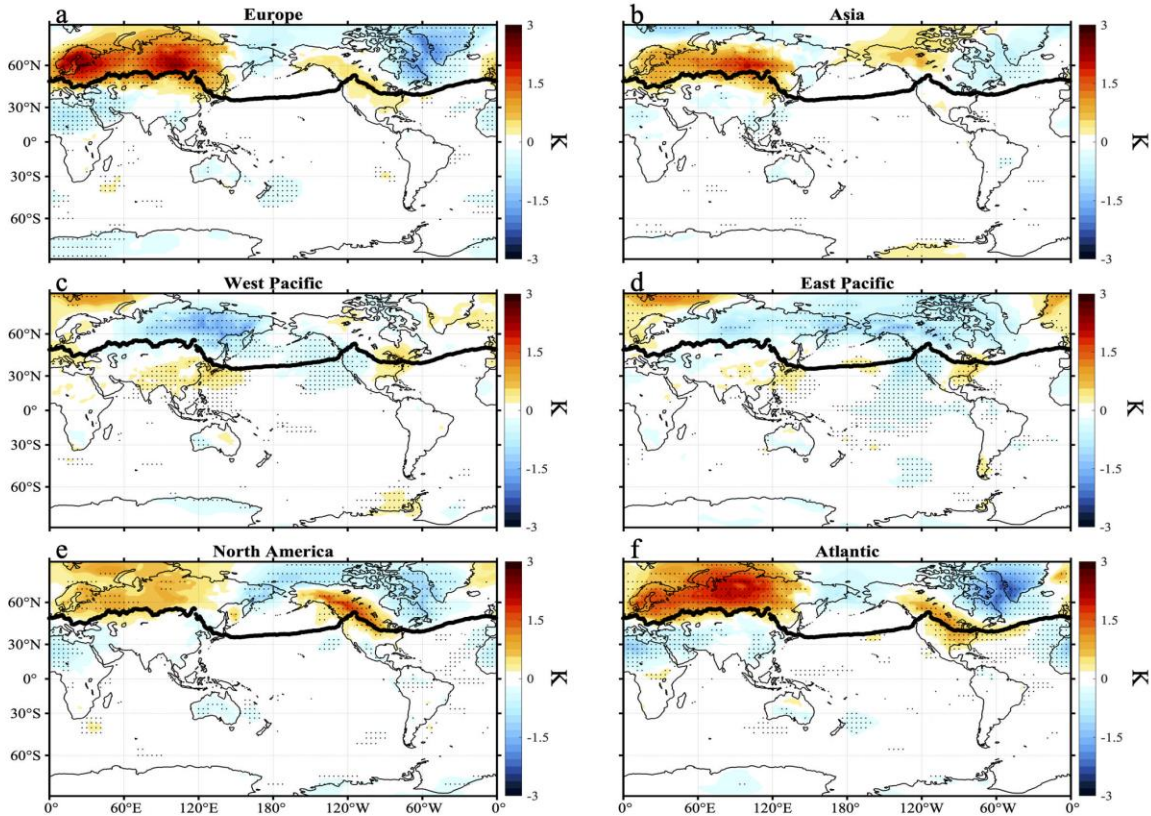
253

254 To interpret the correlations shown in Fig. 2, we now examine the physical processes
255 associated with variability in the positions and strengths of the jets. To do this, we regress
256 monthly anomalies of OLR and surface temperature onto each of our four jet indices (PFJ
257 position, PFJ strength, STJ position, STJ strength). Before the regression analysis, we remove
258 the seasonal cycle of each timeseries and normalize the jet indices by subtracting the
259 climatological mean and then dividing by the standard deviation. Results for the PFJ and STJ
260 are shown in the following two subsections. We note that regressions on the distance between
261 the two jets (i.e., the difference in the PFJ and STJ latitudes) are generally dominated by the
262 processes that govern the PFJ position, which has a greater standard deviation at most longitudes
263 (Fig. 1a). Only over the eastern Pacific Ocean and Atlantic Ocean do processes that govern both
264 the PFJ and STJ position play comparable roles in affecting the separation distance between the
265 jets.

266 3.1 Polar front jet

267

Regression of surface temperature onto polar jet position (observed)



268

269 **Figure 3.** Regression of wintertime monthly surface temperature anomalies onto six different
 270 regions' PFJ position in observations. Patterns correspond to surface temperature anomalies
 271 associated with a 1 standard deviation poleward shift of the polar front jet in each region. Thick
 272 black lines on each panel are climatological PFJ positions in observations as shown in Fig. 1a.
 273 Stippling indicates that regression patterns are statistically significant at the 95% level according
 274 to a two-tailed Student's t-test. The model version of this figure is shown in Fig. S1 in the
 275 supplementary material.

276

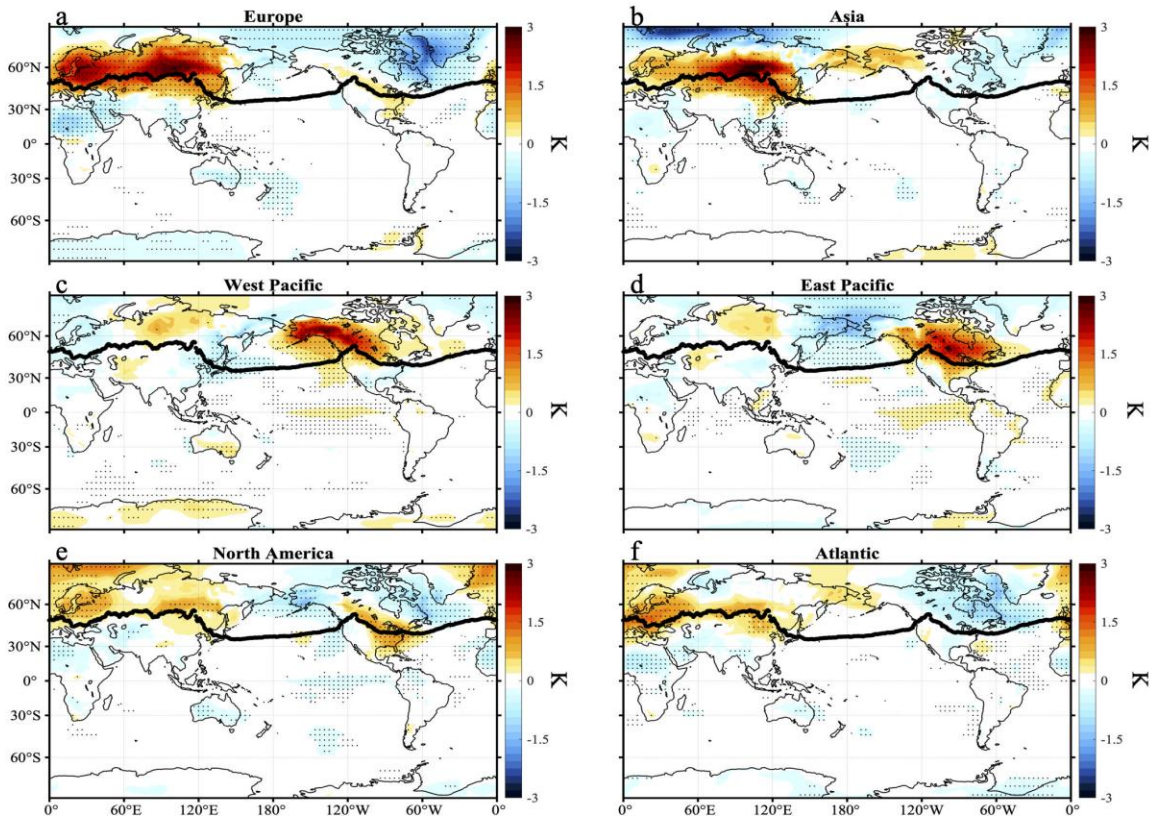
277 Figure 3 shows the regressions of observed wintertime surface temperature anomalies

278 onto the position of the PFJ in six regional sectors (as defined in section 2.2). The surface
279 temperature anomalies shown in each panel correspond to a one standard deviation poleward
280 shift of the PFJ in each of the six regional sectors. Based on idealized aqua-planet simulations,
281 we expect the location of the polar front jet to be controlled closely by shifts in local
282 baroclinicity (Brayshaw, Hoskins, & Blackburn, 2008). This is indeed the case in Fig. 3 in the
283 Asia, West Pacific, and North America sectors. In Asia, the climatological PFJ position is around
284 53°N (Fig. 1), so an anomalously warm Eurasian continent is correlated with a shift in the
285 maximum baroclinicity further poleward, which is consistent with a poleward Asian PFJ shift
286 (Fig. 3b). Likewise, in North America, the climatological PFJ position is oriented from
287 northwest-to-southeast to the east of the Rocky Mountains (Fig. 1a), so anomalous warming over
288 the interior of the North American continent is linked with a shift of the maximum baroclinicity
289 and North American PFJ further poleward (Fig. 3e). Alternatively, because the West Pacific PFJ
290 is located at around 40°N to the south of eastern Russia (Fig. 1a), anomalous cooling over the
291 continent to the north shifts the maximum baroclinicity and West Pacific PFJ further poleward
292 (Fig. 3c).

293 In other regions, the jet position appears to be closely linked to well-known global
294 teleconnection patterns and less clearly to fluctuations in surface baroclinicity at the same
295 longitude. For example, the surface temperature anomalies associated with poleward shifts in
296 the PFJ in the Atlantic and European sectors closely resemble those associated with the positive
297 phase of the North Atlantic Oscillation (NAO), which is characterized by above-normal
298 temperatures over northern Europe and below-normal temperatures over Greenland and Eastern
299 Canada (Hurrell, 1995). A positive NAO signature is also weakly seen for the North American
300 PFJ, suggesting that poleward shifts in the North American PFJ are affected by both the NAO

301 and changes in local surface baroclinicity over the continent. In the eastern Pacific sector, the
 302 surface temperature anomalies associated with a poleward shift in the PFJ closely resemble those
 303 associated with the Pacific-North America pattern (PNA; Wallace & Gutzler, 1981; Yu & Lin,
 304 2019).

Regression of surface temperature onto polar jet strength (observed)



305
 306 **Figure 4.** As in Fig. 3, but for the PFJ strength. The model version of this figure is shown in Fig.
 307 S2 in the supplementary material.

308
 309 Figure 4 shows analogous results to Fig. 3, but for the PFJ strength. The regression
 310 patterns of surface temperature anomalies onto polar jet strength (Fig. 4) are similar to that of
 311 polar jet position (Fig. 3) for Europe, Asia, and North America, but very different in the Pacific.
 312 This suggests that similar processes control the PFJ position and intensity over the continents,

313 but not necessarily over the oceans (see also Fig. 2c). As for the PFJ strength in the Pacific
314 sector, the surface temperature anomalies associated with PFJ intensification closely resemble
315 those associated with the warm phase of the El Niño-Southern Oscillation (ENSO; Halpert &
316 Ropelewski, 1992; Ropelewski & Halpert, 1989). Intensification of the western and eastern
317 Pacific PFJ is associated with enhanced convection (anomalously low OLR) in the eastern
318 tropical Pacific Ocean and suppressed convection (anomalously high OLR) in the western
319 tropical Pacific Ocean (Fig. S3). Alternatively, intensification of the North American PFJ is
320 associated with the cool (La Niña) phase of ENSO (Fig. S3). Intensification of the PFJ in other
321 regions is not associated with significant variations in tropical convection (Fig. S3), and
322 variability in tropical convection also has little to no correlation with variability in PFJ position
323 in any region (not shown).

324 3.2 Subtropical jet

325

326 Figures 5 and 6 show the regressions of observed wintertime OLR anomalies onto the
327 position and strength of the STJ in six regional sectors (as defined in section 2.2). The OLR
328 anomalies shown in each panel correspond to a one standard deviation poleward shift (Fig. 5) or
329 strengthening (Fig. 6) of the STJ in each of the six regional sectors. We also examined
330 regressions of wintertime surface temperature anomalies onto the position and strength of the
331 STJ, but found few significant relationships (not shown).

332 Previous studies have concluded that tropical convection plays a critical role in forcing
333 the position and strength of the STJ locally, particularly over the Pacific sector where El Niño is
334 known to strongly modify the subtropical jet (Gallego et al., 2005; Lu et al., 2008; Seager et al.,
335 2003). Over the western Pacific, enhanced convection is associated with a strengthening and

336 poleward shift of the STJ (Figs. 5c and 6c), consistent with the idealized model results of Lee
337 and Kim (2003) and Son and Lee (2005) and the correlation between western Pacific STJ
338 latitude and speed in Fig. 2d. Over the eastern Pacific, there is a robust relationship between
339 enhanced convection (an El Niño-like pattern) and a strengthened STJ, but there is only a weak
340 relationship between local convection and the STJ position (Figs. 5d and 6d). Additionally, there
341 is a robust relationship between a strengthened STJ over Asia and enhanced convection over the
342 same longitude band (i.e., over the northern Indian Ocean).

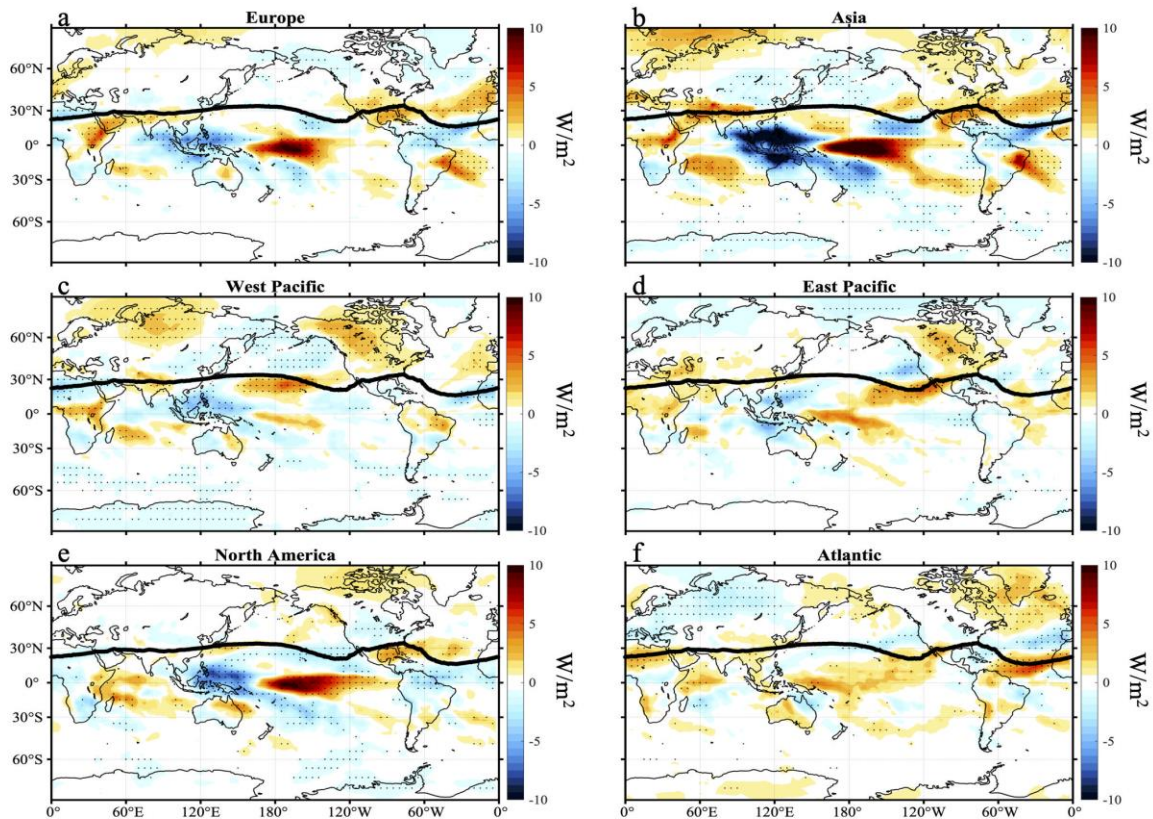
343 At most other longitudes, the variability in the STJ latitude and strength is more affected
344 by teleconnections from remote tropical convection anomalies over the Pacific basin than by
345 tropical convection anomalies at the same longitude. Figure 5 shows that a poleward shift of the
346 STJ over Europe, Asia, and North America is associated with enhanced convection over western
347 tropical Pacific Ocean (i.e., a La Niña-like pattern). This La Niña-like pattern is strongest for
348 North America, indicating a large influence of ENSO on the position of the North American STJ,
349 which is consistent with the well-known teleconnections of ENSO over North America (Cook &
350 Schaefer, 2008; Eichler & Higgins, 2006; Ropelewski & Halpert, 1989; Smith, Green, Leonardi,
351 & O'Brien, 1998). As for the STJ strength, Figure 6 shows that enhanced convection in the
352 eastern tropical Pacific Ocean (i.e., an El Niño-like pattern) is associated with a strengthened STJ
353 over North America. Because enhanced convection in the western tropical Pacific Ocean is
354 associated with a strengthened PFJ over North America (Fig. S3), there is a negative correlation
355 between PFJ and STJ strength over North America (Fig. 2f). Enhanced convection in the western
356 tropical Pacific Ocean is also associated with a strengthened STJ in Europe (see also positive
357 correlations between STJ position and strength in Europe in Fig. 2d).

358 To summarize these relationships, the left column of Figure 7 shows the regression

359 coefficients of observed tropical (5°N-5°S) OLR anomalies onto indices of the STJ position and
360 strength calculated at every longitude (as shown for the climatology in Fig. 1). In other words,
361 for each longitude on the y-axis in Fig. 7, the horizontal line at that y-value shows the zonal cross
362 section of tropical OLR anomalies associated with STJ variability at that longitude. Figure 7
363 reveals that the STJ variability at nearly all longitudes is associated with a dipole of OLR
364 anomalies over the tropical Pacific Basin. This figure shows the dominance of ENSO (rather
365 than local tropical convection) in governing STJ variability globally.

366 Consistent with Fig. 5, Fig. 7a reveals that a La Niña-like pattern of anomalous tropical
367 convection is associated with a poleward shift of the subtropical jet from the eastern Atlantic
368 Ocean to the east coast of Asia, and over North America. Consistent with Fig. 6, Fig. 7c reveals
369 that enhanced tropical convection from the western Indian Ocean to the eastern Pacific Ocean
370 strengthens the STJ at that longitude. A La Niña-like pattern of anomalous tropical convection
371 also strengthens the STJ over the eastern Atlantic Ocean and Europe, but an El Niño-like pattern
372 of anomalous tropical convection strengthens the STJ over North America. In other words, La
373 Niña strengthens the subtropical jet from the western Pacific Ocean to the eastern Atlantic
374 Ocean, and El Niño strengthens the subtropical jet from the central Pacific Ocean to the western
375 Atlantic Ocean (Seager et al., 2003).

Regression of OLR onto subtropical jet position (observed)



376

377 **Figure 5.** Regression of wintertime monthly OLR anomalies onto six different regions'

378 subtropical jet position in observations. Patterns correspond to OLR anomalies associated with a

379 1 standard deviation of poleward shift of the subtropical jet in each region. Thick black lines on

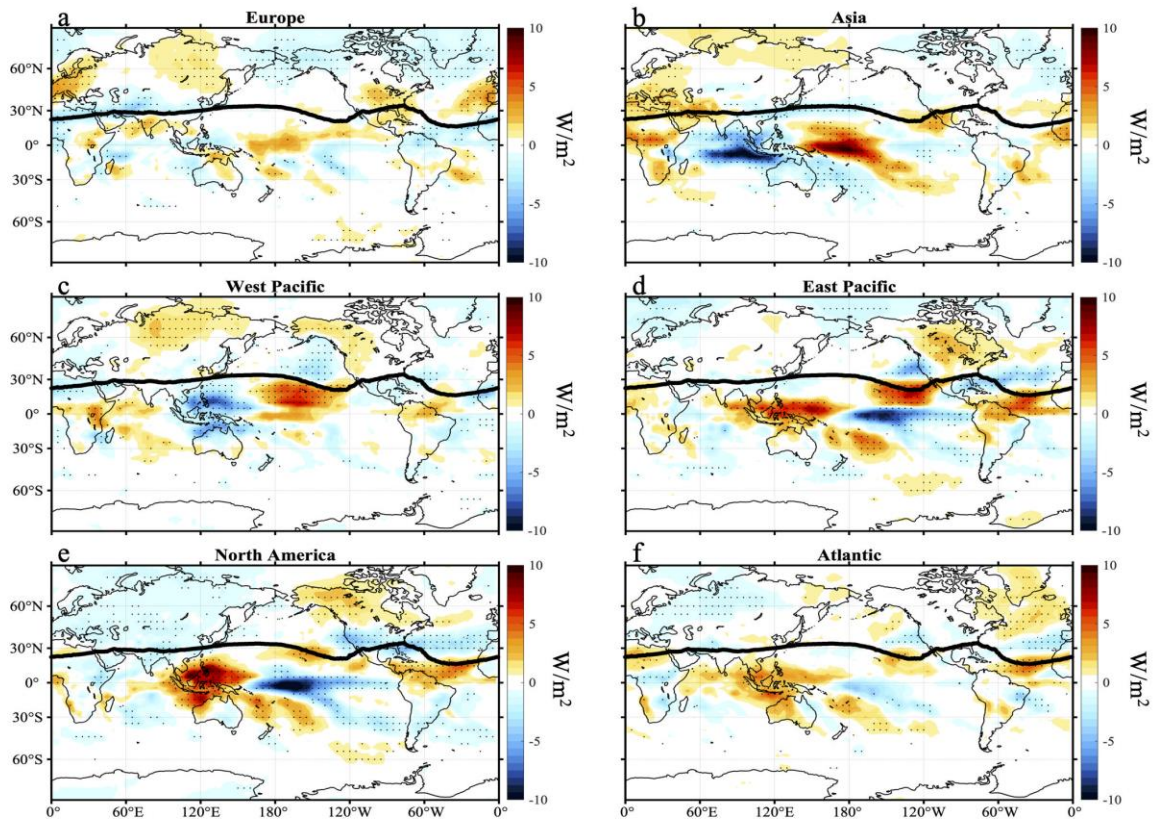
380 each panel are climatological STJ positions in observations as shown in Fig. 1a. Stippling

381 indicates that regression patterns are statistically significant at the 95% level according to a two-

382 tailed Student's t-test. The model version of this figure is shown in Fig. S4 in the supplementary

383 material.

Regression of OLR onto subtropical jet strength (observed)



384

385 **Figure 6.** As in Fig. 5, but for STJ strength. The model version of this figure is shown in Fig. S5
 386 in the supplementary material.

387 **4. Comparison between models and observations**

388 In this section, we compare the observed variability in the position and strength of the jets
 389 (as documented in Section 3) with that from CMIP6 models. Model results for the regressions
 390 on PFJ position and strength are shown in Figs. S1 and S2, and model results for the regressions
 391 on STJ position and strength are shown in Figs. S4 and S5. The model regressions of surface
 392 temperature anomalies onto the PFJ position and strength are very similar to those shown for
 393 observations (Figs. 3-4), but the model regressions of OLR anomalies onto STJ position and

394 strength differ significantly from observations (Figs. 5-6). For that reason, in this section, we
395 focus on the comparison of the STJ variability between observations and CMIP6 models.

396 To summarize the model biases in STJ variability, the right column of Fig. 7 shows the
397 CMIP6 multi-model mean regression coefficients of tropical (5°N-5°S) OLR anomalies onto
398 indices of the STJ position and strength calculated at every longitude (as shown in the left
399 column for observations). Consistent with observations (Figs. 5-6), it is worth noting that the
400 STJ at each longitude in the multi-model mean is not primarily sensitive to OLR at its own
401 longitude, but rather responds to tropical OLR anomalies in the Pacific. However, for the OLR
402 anomalies associated with a poleward shift in the STJ, tropical convection in the models is
403 displaced westward for Europe, Asia, and the western tropical Pacific when compared to
404 observations (Figs. 7a-b). Additionally, large discrepancies between the observed and model
405 patterns occur in the North America. Over North America in observations, a La Niña-like pattern
406 in anomalous tropical convection is associated with a poleward shift of the STJ position but this
407 pattern is not shown in models. For the OLR anomalies associated with a strengthening of the
408 STJ (Figs. 7c-d), most models capture the observed relationship between La Niña and a
409 strengthened STJ over the western Pacific Ocean, and between El Niño and a strengthened STJ
410 over the eastern Pacific Ocean and North America (see the prominent quadrupole pattern in the
411 left-center of panels c and d). However, most models fail to capture the observed relationship
412 between tropical convection and the STJ strength over the eastern Atlantic Ocean and Eurasia.

413 We now discuss the possible causes of these model-observation discrepancies shown in
414 Fig. 7. As discussed above, models agree that a La Niña-like pattern in anomalous tropical
415 convection is associated with a poleward shift of the STJ position in the Eurasian and western
416 Pacific sectors, but the dipole of OLR anomalies is shifted to the west in the multi-model-mean

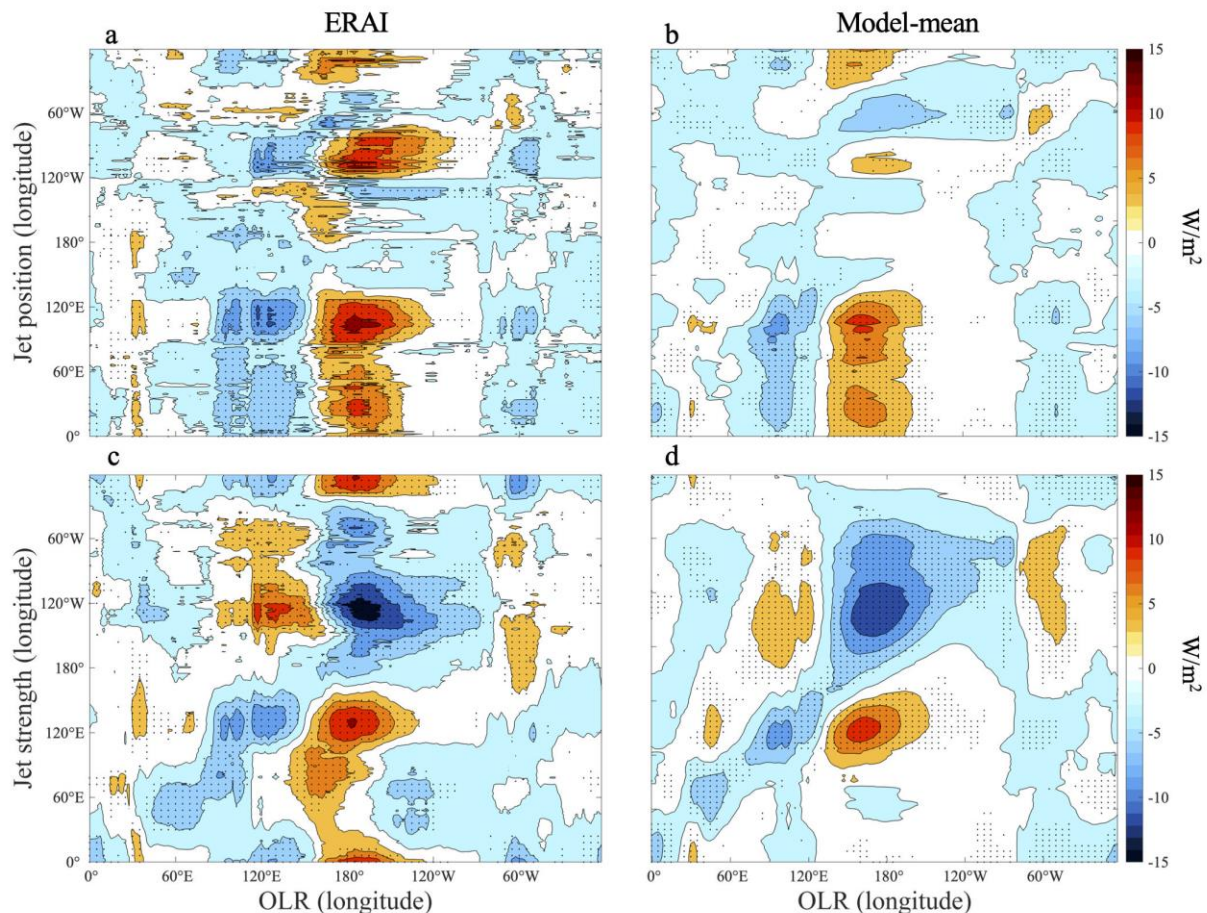
417 compared to observations (Figs. 7a-b). To illustrate this more clearly, the top row of Fig. 8 shows
418 the regressions of OLR anomalies onto the STJ position in the Asian sector (as shown in Figs. 5
419 and S4, but zoomed in to show greater detail). In particular, notice that the region of enhanced
420 convection in the multi-model-mean is narrower and confined to longitudes west of the
421 Philippines, and that the region of suppressed convection along the Equator in the multi-model-
422 mean extends much further to the west over New Guinea (Fig. 8b).

423 One reason for the westward shift of the La Niña-like pattern in models could be that the
424 climatological OLR field in CMIP6 models is different from that in observations, as some
425 previous studies have documented that ENSO diversity is associated with the tropical Pacific
426 background state (Capotondi et al., 2015; Choi, An, Kug, & Yeh, 2011; Chung & Li, 2013). The
427 observed and multi-model-mean OLR climatology in the equatorial Pacific is shown in Fig. 8c
428 and Fig. 8d. The equatorial low OLR region in observations in the western Pacific is wider and
429 extends further eastward than in the multi-model-mean climatology. To illustrate this better, we
430 also plot the cross-section of observed and multi-model-mean climatological OLR at the Equator
431 as a function of longitude in Fig. 8e.

432 In Fig. 9, we show the correlation between the position of the climatological low OLR
433 region along the Equator in the western Pacific Ocean (as shown in Fig. 8e) and the position of
434 the OLR anomalies associated with a poleward STJ shift over the Asia sector (as shown in Figs.
435 8a and 8b) across CMIP6 models. The climatological low OLR region is defined as the region
436 where OLR is smaller than 255 W m^{-2} , and we define the position of the low OLR region as the
437 mid-point longitude of the low OLR region in the equatorial western Pacific. The results are not
438 sensitive to the exact choice of threshold value (i.e., values between 250 and 270 W m^{-2} give
439 similar results). The position of the OLR associated with a poleward STJ shift over the Asia

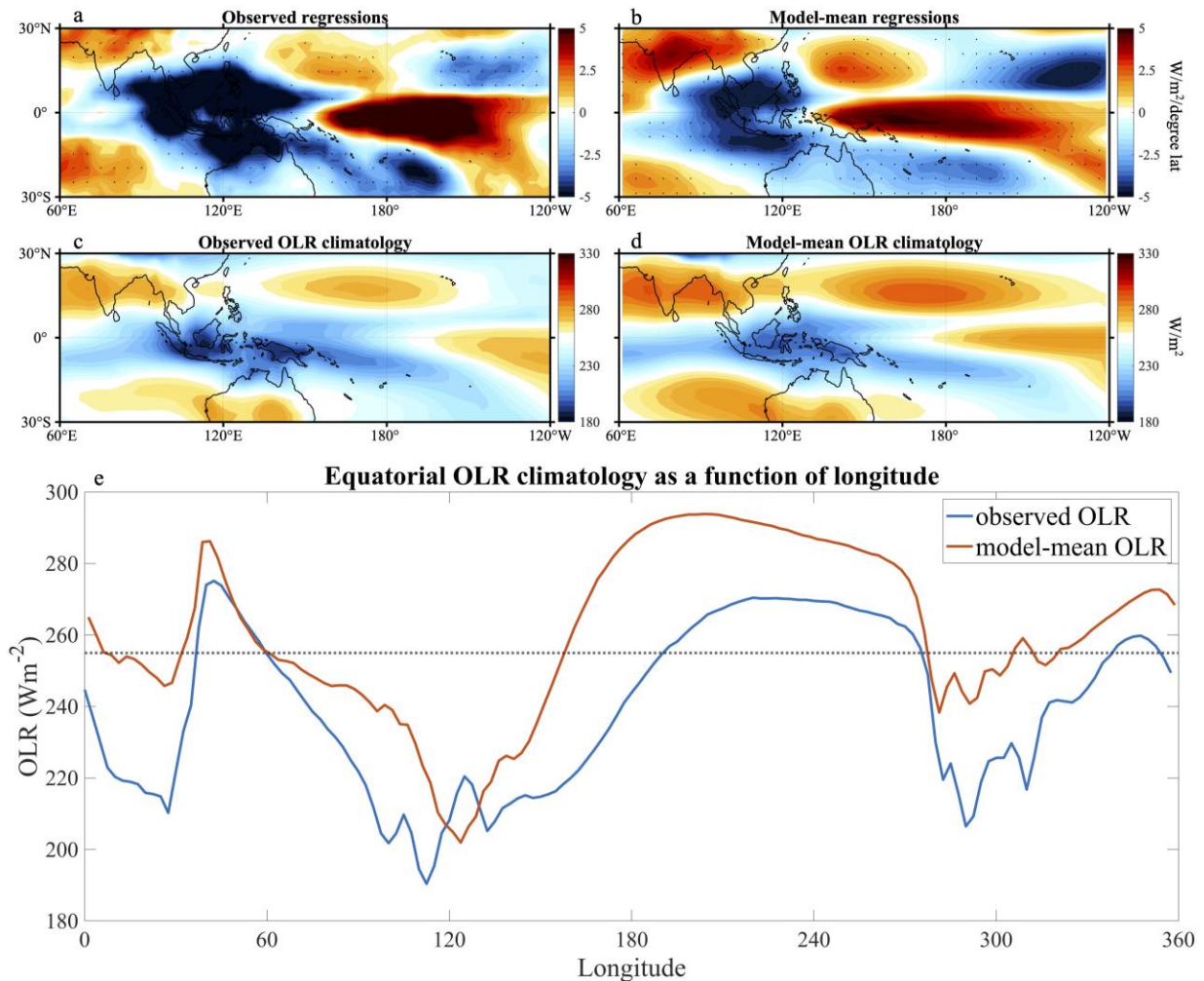
440 sector, which we refer to as the “La Niña pattern index”, is defined as the transition longitude
 441 between 120°E-180°E where the regression coefficient of OLR to Asian STJ position (as shown
 442 in Figs. 8a and 8b) averaged over 10° S to 20° N crosses zero. The positive relationship between
 443 the midpoint of the climatological low OLR region and La Niña pattern index (Pearson
 444 correlation coefficient r is 0.80) indicates that the westward La Niña-like pattern in models’
 445 tropical convection associated with a poleward STJ shift over the Europe-Asia-Pacific sector can
 446 be attributed to the biased OLR climatology in the tropical western Pacific Ocean in many
 447 models. The western Pacific tropical convection is centered further to the west than observations
 448 in nearly all of the models and thus causes a westward shift of the La Niña-like pattern of
 449 anomalous tropical convection.

Regression of tropical OLR onto subtropical jet indices at all longitudes



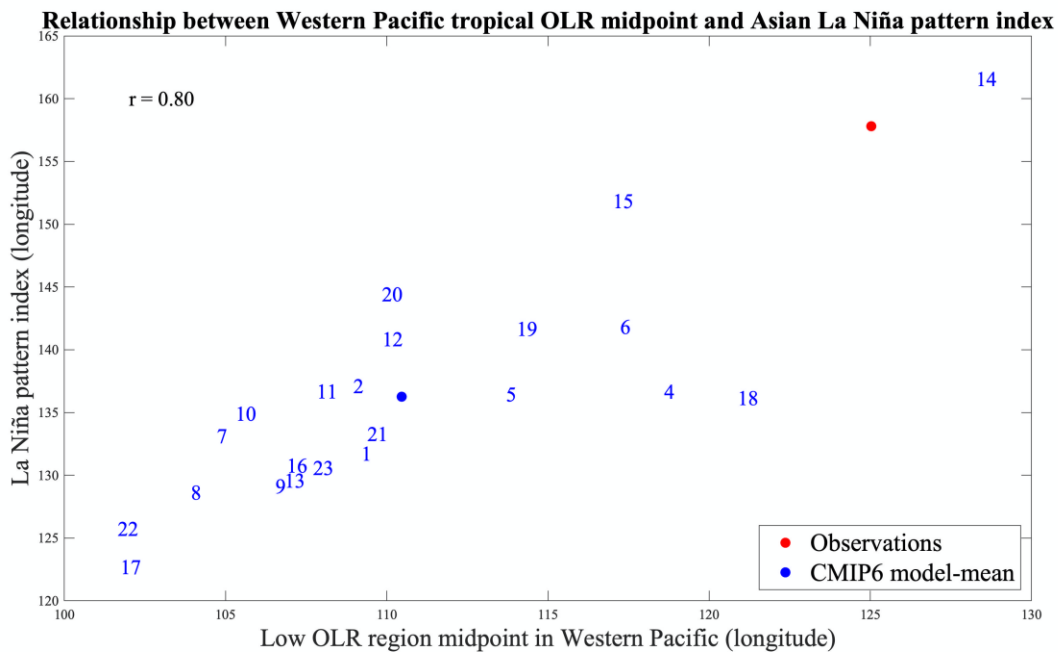
450

451 **Figure 7.** Regression of the wintertime monthly tropical OLR (5°S - 5°N) anomalies onto
 452 subtropical jet indices at all longitudes. (a) and (b) are regression coefficients for subtropical jet
 453 position; (c) and (d) are regression coefficients for subtropical jet strength. The left column
 454 shows results for observations, and the right column shows results for the CMIP6 multi-model-
 455 mean. Color shading represents the regression coefficient of OLR at the longitude on the x-axis
 456 to the subtropical jet index at the longitude on y axis. For (a) and (c), stippling indicates that
 457 regression patterns are statistically significant at the 95% level according to a two-tailed
 458 Student's t-test. For (b) and (d), stippling indicates that more than 80% of models agree on the
 459 sign of the regression coefficients.



460

461 **Figure 8.** (a) and (b) are regressions of monthly wintertime OLR anomalies to the Asian STJ
 462 position for observations and the CMIP6 multi-model mean (reproduced from the second panels
 463 of Figure 5 and Figure S4 but zoomed in and with different color scales). (c) and (d) are the
 464 wintertime OLR climatology for observations and the CMIP6 multi-model mean. (e) is the
 465 observed and multi-model-mean wintertime OLR climatology at the Equator as a function of
 466 longitude. The blue line shows the observed OLR, while the red line shows the model-mean
 467 OLR. The dashed black line shows the 255 Wm^{-2} OLR value, below which is defined as low
 468 OLR.
 469



470
 471 **Figure 9.** Scatter plot between the midpoint of the wintertime climatological low OLR region
 472 over the western Pacific and the La Niña pattern index. The La Niña pattern index is defined as
 473 the transition longitude between 120°E - 180°E where the regression coefficient of wintertime
 474 monthly OLR anomalies to the Asian STJ position (as shown in Figs. 8a and 8b) averaged over
 475 10°S to 20°N crosses zero. The midpoint of the climatological low OLR region is defined as

476 the mid-point longitude of the low OLR region in equatorial Western Pacific (as shown in Fig.
477 8e). The low OLR region is defined where the OLR is smaller than 255 W m^{-2} . Numbers on the
478 scatterplot correspond to the models listed in Table. S1. The blue dot represents multi-model-
479 mean, while the red dot is for observations.

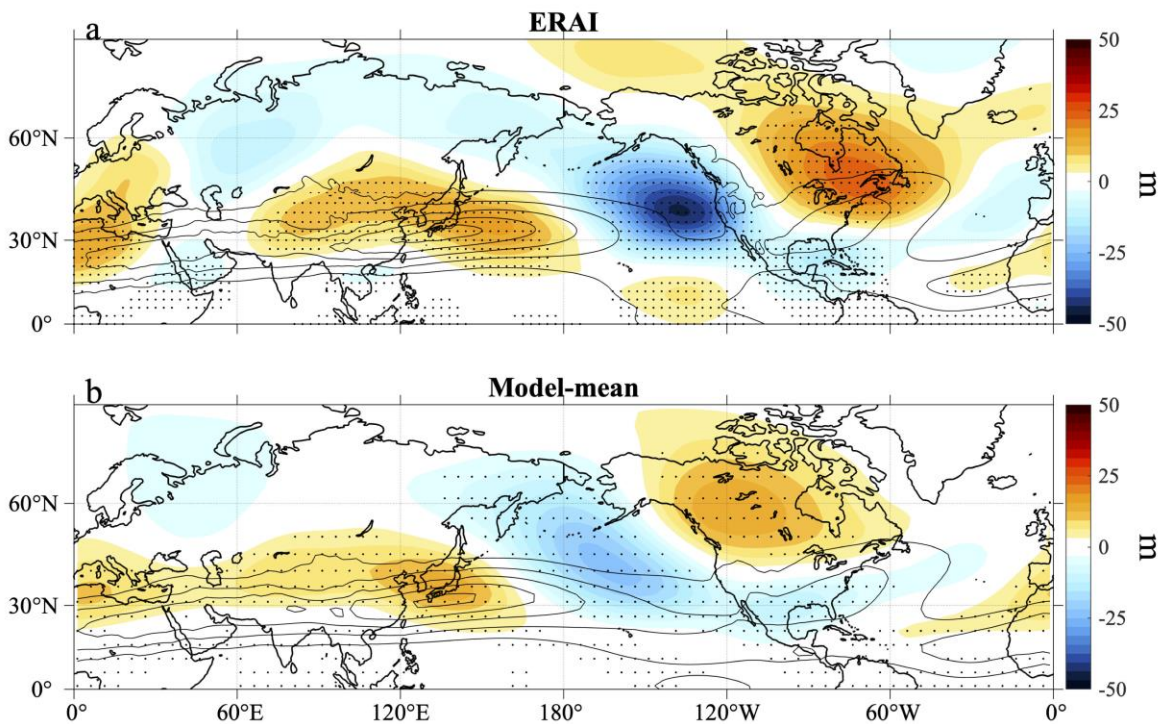
480

481 Another key discrepancy between observations and models shown in Fig. 7 is that models
482 fail to capture the linkage between a La Niña-like pattern of anomalous tropical convection and
483 the poleward shift of the STJ over North America (Fig. 7b). Given the biased OLR climatology
484 in models, it seems plausible that different Rossby wave trains would be excited by tropical
485 convection at different locations associated with El Niño and La Niña patterns in observations
486 and models (Jiménez-Esteve & Domeisen, 2018). To illustrate this, Figure 10 shows the
487 regressions of eddy geopotential height anomalies at 500 hPa onto the Niño 3.4 index (i.e., sea
488 surface temperatures averaged over 5°N - 5°S , 170°W - 120°W) for both observations and the
489 CMIP6 multi-model mean. Here, the term eddy geopotential height anomalies means that both
490 the zonal mean and seasonal cycle has been removed from the geopotential height data. As
491 shown in Fig. 10a, the wave train excited by anomalous tropical convection in observations is
492 further south and east compared to that in multi-model-mean. Consequently, a north-south
493 dipole of eddy geopotential height anomalies is located directly over the STJ in eastern North
494 America in observations, but not in models.

495 Finally, we noted above that models fail to capture the observed relationship between a
496 La Niña-like pattern of anomalous tropical convection and STJ strength over the eastern Atlantic
497 and European sectors (Fig. 7d). As shown in Fig. 10a, the wave train associated with ENSO in
498 observations propagates poleward to Alaska and Canada and then back equatorward toward the

499 North Atlantic and Western Europe, where it projects onto the STJ in this region. In the multi-
 500 model mean, the wave train associated with ENSO is shifted further westward and thus returns
 501 equatorward over the central Atlantic Ocean (Fig. 10b). However, ENSO's impacts in the North
 502 Atlantic may be highly variable and unstable (note lack of significance in Fig. 10 over North
 503 Atlantic), which means that the observed teleconnections in this sector may be highly sensitive to
 504 the time frame we choose (Greatbatch, Lu, & Peterson, 2004).

Regression of geopotential height anomaly onto Niño 3.4 index



505
 506 **Figure 10.** Regression of wintertime monthly eddy 500 hPa geopotential height anomalies (i.e.,
 507 with both the seasonal cycle and zonal-mean field removed) onto the Niño 3.4 index in
 508 observations (a) and the CMIP6 multi-model mean (b). The Niño 3.4 index is defined as SST
 509 anomalies averaged across 5°N-5°S, 170°W-120°W. Stippling in (a) indicates that regression
 510 patterns are statistically significant at the 95% level according to a two-tailed Student's t-test,
 511 and stippling in (b) indicates that more than 80% of models agree with the sign of regression

512 coefficients. Black contours indicate the climatology of zonal wind difference fields (250 hPa
513 zonal wind – 850 hPa zonal wind), which are used to define the STJ position. Contours are
514 shown at 20, 30, 40, 50 and 60 m/s.

515

516 **5. Summary and conclusions**

517 The position and intensity of the polar front and subtropical jet streams in Northern
518 Hemisphere winter exhibit large spatial and temporal variance. Some previous studies (e.g., Lee
519 & Kim, 2003; Son & Lee, 2005) have provided insight into the processes that control the
520 variability of the polar front and subtropical jets, but most of these studies have relied on
521 idealized aqua-planet models with no zonal asymmetries in the jets. Although correlations
522 among variations in the strength and position of the jets could be anticipated from such idealized
523 modeling studies, variability in the position and strength of the zonal-mean STJ and PFJ actually
524 exhibit few significant correlations in observations and comprehensive global climate models
525 (Fig. 2; Solomon et al. 2016; Waugh et al. 2018; Menzel et al. 2019; Davis & Birner 2017). The
526 lack of significant correlations among the position and strength of the jets in the zonal-mean
527 mask significant correlations among those of the jets that occur on the regional level (Fig. 2),
528 which highlights the need to examine the interannual variability of the jets and the underlying
529 mechanisms at individual longitudes.

530 In this study, we find a close relationship between the observed variability in the position
531 and strength of the STJ and tropical outgoing longwave radiation (OLR), and between the
532 observed variability in position and strength of the PFJ with mid-latitude surface temperature
533 gradients during the NH winter season. Local changes in surface baroclinicity are associated with
534 variability in the position and strength of the NH PFJ, particularly over Asia, western Pacific and

535 North America (Figs. 2-3). In other regions, global-scale teleconnection patterns (NAO and
536 PNA) play a key role in modulating the position and strength of the PFJ, particularly over the
537 North Atlantic Ocean and Europe. Variations in tropical convection over the Pacific Ocean are
538 linked to variations in the strength and position of the NH STJ at almost all longitudes, with
539 different phases of the El Niño-Southern Oscillation (ENSO) associated with the poleward shift
540 and strengthening of the subtropical jet in different regions (Figs. 4-5).

541 CMIP6 models generally capture these observed relationships, but for the STJ variability,
542 the models' tropical convection is often displaced westward when compared to observations
543 (Figs. 7-8). This difference between models and observations can be attributed to the biased
544 OLR climatology over the tropical Western Pacific Ocean in many models, with climatological
545 convection in models displaced westward with respect to observations (Figs. 8-9). The displaced
546 tropical convection in models excites different paths of Rossby wave propagation, making
547 downstream ENSO teleconnections on the STJ over North America, the Atlantic Ocean, and
548 Europe different compared to observations.

549 Our study examines observed characteristics of the NH wintertime STJ and PFJ at all
550 longitudes and provides insight into the processes governing their interannual variability over the
551 last four decades. Future work could extend this study to the Southern Hemisphere, or investigate
552 the mechanisms governing the jet variability in other seasons in the NH. It may also be
553 worthwhile to examine whether the mechanisms governing the latitudes, strengths, and
554 meridional separation between the jets change in the future as the climate warms. Although
555 climate models show a robust poleward shift of the PFJ in a warming climate (e.g., Barnes &
556 Polvani 2013), the STJ does not show a consistent poleward or equatorward shift, at least in the
557 zonal mean (Davis & Birner 2017; Waugh et al. 2018; Menzel et al. 2019). Recent reanalysis

558 data also show poleward trends in the PFJ latitude (e.g., Allen and Kovilakam 2017; Grise et al.
559 2018), but inconsistent trends in the STJ latitude (Maher et al., 2020; Manney & Hegglin, 2018).
560 Not only does this suggest that the mechanisms driving the responses of the STJ and PFJ to
561 climate change could be very different (as discussed by Menzel et al. 2019), but it also implies
562 that the character of the general circulation (i.e., preference for a merged jet at some longitudes
563 and two distinct jets at other longitudes) may change as the climate warms, hence modulating
564 interannual variability of the jets and the associated behavior of synoptic weather events.

565

566 **Acknowledgments**

567 We acknowledge the World Climate Research Programme, which, through its Working Group
568 on Coupled Modelling, coordinated and promoted CMIP6. We thank the climate modeling
569 groups for producing and making available their model output, the Earth System Grid Federation
570 (ESGF) for archiving the data and providing access, and the multiple funding agencies who
571 support CMIP6 and ESGF. We also thank Carlee Kleppin (University of Virginia) for her initial
572 work on this topic. This material is based in part upon work supported by the National Science
573 Foundation under Grant No. AGS-1752900.

574 CMIP6 model output is freely available from the Lawrence Livermore National Laboratory
575 (<https://esgf-node.llnl.gov/search/cmip6/>). ERA-Interim reanalysis data are freely available from
576 the European Centre for Medium-Range Weather Forecasts

577 (<https://apps.ecmwf.int/datasets/data/interim-full-moda/>;

578 <https://cds.climate.copernicus.eu/#!/search?text=ERA5&type=dataset>). Monthly outgoing

579 longwave radiation (OLR) datasets are freely available from NOAA Physical Sciences

580 Laboratory (https://psl.noaa.gov/data/gridded/data.interp_OLR.html).

581 **References**

- 582 Adam, O., Grise, K. M., Staten, P., Simpson, I. R., Davis, S. M., Davis, N. A., ... Birner, T.
583 (2018). The TropD software package: Standardized methods for calculating Tropical Width
584 Diagnostics. *Geoscientific Model Development Discussions*, 1–35.
585 <https://doi.org/10.5194/gmd-2018-124>
- 586 Afargan, H., & Kaspi, Y. (2017). A Midwinter Minimum in North Atlantic Storm Track
587 Intensity in Years of a Strong Jet. *Geophysical Research Letters*, 44(24), 12,511–12,518.
588 <https://doi.org/10.1002/2017GL075136>
- 589 Allen, R. J., & Kovilakam, M. (2017). The role of natural climate variability in recent tropical
590 expansion. *Journal of Climate*, 30(16), 6329–6350. [https://doi.org/10.1175/JCLI-D-16-](https://doi.org/10.1175/JCLI-D-16-0735.1)
591 [0735.1](https://doi.org/10.1175/JCLI-D-16-0735.1)
- 592 Archer, C. L., & Caldeira, K. (2008). Historical trends in the jet streams. *Geophysical Research*
593 *Letters*, 35(8), 1–6. <https://doi.org/10.1029/2008GL033614>
- 594 Athanasiadis, P. J., Wallace, J. M., & Wettstein, J. J. (2010). Patterns of wintertime jet stream
595 variability and their relation to the storm tracks. *Journal of the Atmospheric Sciences*, 67(5),
596 1361–1381. <https://doi.org/10.1175/2009JAS3270.1>
- 597 Bals-Elsholz, T. M., Atallah, E. H., Bosart, L. F., Wasula, T. A., Cempa, M. J., & Lupo, A. R.
598 (2001). The wintertime southern hemisphere split jet: Structure, variability, and evolution.
599 *Journal of Climate*, 14(21), 4191–4215. [https://doi.org/10.1175/1520-](https://doi.org/10.1175/1520-0442(2001)014<4191:TWSHSJ>2.0.CO;2)
600 [0442\(2001\)014<4191:TWSHSJ>2.0.CO;2](https://doi.org/10.1175/1520-0442(2001)014<4191:TWSHSJ>2.0.CO;2)
- 601 Barnes, E. A., & Hartmann, D. L. (2010). Influence of eddy-driven jet latitude on North Atlantic
602 jet persistence and blocking frequency in CMIP3 integrations. *Geophysical Research*
603 *Letters*, 37(23). <https://doi.org/10.1029/2010GL045700>

- 604 Barnes, E. A., & Polvani, L. (2013). Response of the midlatitude jets, and of their variability, to
605 increased greenhouse gases in the CMIP5 models. *Journal of Climate*, 26(18), 7117–7135.
606 <https://doi.org/10.1175/JCLI-D-12-00536.1>
- 607 Brayshaw, D. J., Hoskins, B., & Blackburn, M. (2008). The Storm-Track Response to Idealized
608 SST Perturbations in an Aquaplanet GCM. *Journal of the Atmospheric Sciences*, 65(9),
609 2842–2860. <https://doi.org/10.1175/2008JAS2657.1>
- 610 Capotondi, A., Wittenberg, A. T., Newman, M., Di Lorenzo, E., Yu, J. Y., Braconnot, P., ...
611 Yeh, S. W. (2015). Understanding enso diversity. *Bulletin of the American Meteorological*
612 *Society*, 96(6), 921–938. <https://doi.org/10.1175/BAMS-D-13-00117.1>
- 613 Ceppi, P., & Hartmann, D. L. (2013). On the speed of the eddy-driven jet and the width of the
614 hadley cell in the southern hemisphere. *Journal of Climate*, 26(10), 3450–3465.
615 <https://doi.org/10.1175/JCLI-D-12-00414.1>
- 616 Choi, J., An, S. Il, Kug, J. S., & Yeh, S. W. (2011). The role of mean state on changes in El
617 Niño’s flavor. *Climate Dynamics*, 37(5), 1205–1215. [https://doi.org/10.1007/s00382-010-](https://doi.org/10.1007/s00382-010-0912-1)
618 [0912-1](https://doi.org/10.1007/s00382-010-0912-1)
- 619 Christenson, C. E., Martin, J. E., & Handlos, Z. J. (2017). A synoptic climatology of Northern
620 Hemisphere, cold season polar and subtropical jet superposition events. *Journal of Climate*,
621 30(18), 7231–7246. <https://doi.org/10.1175/JCLI-D-16-0565.1>
- 622 Chung, P. H., & Li, T. (2013). Interdecadal relationship between the mean state and El Niño
623 types. *Journal of Climate*, 26(2), 361–379. <https://doi.org/10.1175/JCLI-D-12-00106.1>
- 624 Cook, A. R., & Schaefer, J. T. (2008). The relation of El Niño-Southern Oscillation (ENSO) to
625 winter tornado outbreaks. *Monthly Weather Review*, 136(8), 3121–3137.
626 <https://doi.org/10.1175/2007MWR2171.1>

- 627 Davis, N., & Birner, T. (2016). Climate model biases in the width of the tropical belt. *Journal of*
628 *Climate*, 29(5), 1935–1954. <https://doi.org/10.1175/JCLI-D-15-0336.1>
- 629 Davis, N., & Birner, T. (2017). On the discrepancies in tropical belt expansion between
630 reanalyses and climate models and among tropical belt width metrics. *Journal of Climate*,
631 30(4), 1211–1231. <https://doi.org/10.1175/JCLI-D-16-0371.1>
- 632 Dee, D. P., Uppala, S. M., Simmons, A. J., Berrisford, P., Poli, P., Kobayashi, S., ... Vitart, F.
633 (2011). The ERA-Interim reanalysis: Configuration and performance of the data
634 assimilation system. *Quarterly Journal of the Royal Meteorological Society*, 137(656), 553–
635 597. <https://doi.org/10.1002/qj.828>
- 636 Dickson, R. R., & Namias, J. (1976). North American Influences on the Circulation and Climate
637 of the North Atlantic Sector. *Monthly Weather Review*, 104(10), 1255–1265.
638 [https://doi.org/10.1175/1520-0493\(1976\)104<1255:NAIOTC>2.0.CO;2](https://doi.org/10.1175/1520-0493(1976)104<1255:NAIOTC>2.0.CO;2)
- 639 Eichelberger, S. J., & Hartmann, D. L. (2007). Zonal jet structure and the leading mode of
640 variability. *Journal of Climate*, 20(20), 5149–5163. <https://doi.org/10.1175/JCLI4279.1>
- 641 Eichler, T., & Higgins, W. (2006). Climatology and ENSO-related variability of North American
642 extratropical cyclone activity. *Journal of Climate*, 19(10), 2076–2093.
643 <https://doi.org/10.1175/JCLI3725.1>
- 644 Eyring, V., Bony, S., Meehl, G. A., Senior, C. A., Stevens, B., Stouffer, R. J., & Taylor, K. E.
645 (2016). Overview of the Coupled Model Intercomparison Project Phase 6 (CMIP6)
646 experimental design and organization. *Geoscientific Model Development*, 9(5), 1937–1958.
647 <https://doi.org/10.5194/gmd-9-1937-2016>
- 648 Gallego, D., Ribera, P., Garcia-Herrera, R., Hernandez, E., & Gimeno, L. (2005). A new look for
649 the Southern Hemisphere jet stream. *Climate Dynamics*, 24(6), 607–621.

- 650 <https://doi.org/10.1007/s00382-005-0006-7>
- 651 Greatbatch, R. J., Lu, J., & Peterson, K. A. (2004). Nonstationary impact of ENSO on Euro-
652 Atlantic winter climate. *Geophysical Research Letters*, *31*(2), 4–7.
653 <https://doi.org/10.1029/2003GL018542>
- 654 Grise, K. M., Davis, S. M., Staten, P. W., & Adam, O. (2018). Regional and seasonal
655 characteristics of the recent expansion of the tropics. *Journal of Climate*, *31*(17), 6839–
656 6856. <https://doi.org/10.1175/JCLI-D-18-0060.1>
- 657 Halpert, M. S., & Ropelewski, C. F. (1992). Surface Temperature Patterns Associated with the
658 Southern Oscillation. *Journal of Climate*, *5*(6), 577–593. [https://doi.org/10.1175/1520-
659 0442\(1992\)005<0577:STPAWT>2.0.CO;2](https://doi.org/10.1175/1520-0442(1992)005<0577:STPAWT>2.0.CO;2)
- 660 Handlos, Z. J., & Martin, J. E. (2016). Composite analysis of large-scale environments
661 conducive to western Pacific polar/subtropical jet superposition. *Journal of Climate*, *29*(19),
662 7145–7165. <https://doi.org/10.1175/JCLI-D-16-0044.1>
- 663 Held, I. M. (1975). Momentum Transport by Quasi-Geostrophic Eddies. *Journal of the*
664 *Atmospheric Sciences*, *32*(7), 1494–1497. [https://doi.org/10.1175/1520-
665 0469\(1975\)032<1494:MTBQGE>2.0.CO;2](https://doi.org/10.1175/1520-0469(1975)032<1494:MTBQGE>2.0.CO;2)
- 666 Held, I. M., & Hou, A. Y. (1980). Nonlinear Axially Symmetric Circulations in a Nearly Inviscid
667 Atmosphere. *Journal of the Atmospheric Sciences*, *37*(3), 515–533.
668 [https://doi.org/10.1175/1520-0469\(1980\)037<0515:NASCIA>2.0.CO;2](https://doi.org/10.1175/1520-0469(1980)037<0515:NASCIA>2.0.CO;2)
- 669 Hurrell, J. W. (1995). Decadal Trends in the North Atlantic Oscillation: Regional Temperatures
670 and Precipitation. *Science*, *269*(5224), 676 LP – 679.
671 <https://doi.org/10.1126/science.269.5224.676>
- 672 Jiménez-Esteve, B., & Domeisen, D. I. V. (2018). The tropospheric pathway of the ENSO-North

- 673 Atlantic teleconnection. *Journal of Climate*, 31(11), 4563–4584.
674 <https://doi.org/10.1175/JCLI-D-17-0716.1>
- 675 Kaas, E., & Branstator, G. (1993). The Relationship between a Zonal Index and Blocking
676 Activity. *Journal of Atmospheric Sciences*, 50(18), 3061–3077.
677 [https://doi.org/10.1175/1520-0469\(1993\)050<3061:TRBAZI>2.0.CO;2](https://doi.org/10.1175/1520-0469(1993)050<3061:TRBAZI>2.0.CO;2)
- 678 Kim, H. K., & Lee, S. (2004). The wave-zonal mean flow interaction in the Southern
679 Hemisphere. *Journal of the Atmospheric Sciences*, 61(9), 1055–1067.
680 [https://doi.org/10.1175/1520-0469\(2004\)061<1055:TWMFII>2.0.CO;2](https://doi.org/10.1175/1520-0469(2004)061<1055:TWMFII>2.0.CO;2)
- 681 Koch, P., Wernli, H., & Davies, H. C. (2006). An event-based jet-stream climatology and
682 typology. *International Journal of Climatology*, 26(3), 283–301.
683 <https://doi.org/10.1002/joc.1255>
- 684 Lee, S., & Kim, H. K. (2003). The dynamical relationship between subtropical and eddy-driven
685 jets. *Journal of the Atmospheric Sciences*, 60(12), 1490–1503. [https://doi.org/10.1175/1520-](https://doi.org/10.1175/1520-0469(2003)060<1490:TDRBSA>2.0.CO;2)
686 [0469\(2003\)060<1490:TDRBSA>2.0.CO;2](https://doi.org/10.1175/1520-0469(2003)060<1490:TDRBSA>2.0.CO;2)
- 687 Li, C., & Wettstein, J. J. (2012). Thermally driven and eddy-driven jet variability in reanalysis.
688 *Journal of Climate*, 25(5), 1587–1596. <https://doi.org/10.1175/JCLI-D-11-00145.1>
- 689 Liebmann, B., & Smith, C. A. (1996). Description of a Complete (Interpolated) Outgoing
690 Longwave Radiation Dataset. *Bulletin of the American Meteorological Society*, 77, 1275–
691 1277.
- 692 Lu, J., Chen, G., & Frierson, D. M. W. (2008). Response of the zonal mean atmospheric
693 circulation to El Niño versus global warming. *Journal of Climate*, 21(22), 5835–5851.
694 <https://doi.org/10.1175/2008JCLI2200.1>
- 695 Maher, P., Kelleher, M. E., Sansom, P. G., & Methven, J. (2020). Is the subtropical jet shifting

- 696 poleward? *Climate Dynamics*, 54(3–4), 1741–1759. <https://doi.org/10.1007/s00382-019->
697 05084-6
- 698 Mahlstein, I., Martius, O., Chevalier, C., & Ginsbourger, D. (2012). Changes in the odds of
699 extreme events in the Atlantic basin depending on the position of the extratropical jet.
700 *Geophysical Research Letters*, 39(22), 1–6. <https://doi.org/10.1029/2012GL053993>
- 701 Manney, G. L., & Hegglin, M. I. (2018). Seasonal and regional variations of long-term changes
702 in upper-tropospheric jets from reanalyses. *Journal of Climate*, 31(1), 423–448.
703 <https://doi.org/10.1175/JCLI-D-17-0303.1>
- 704 Menzel, M. E., Waugh, D., & Grise, K. (2019). Disconnect Between Hadley Cell and
705 Subtropical Jet Variability and Response to Increased CO₂. *Geophysical Research Letters*,
706 46(12), 7045–7053. <https://doi.org/10.1029/2019GL083345>
- 707 Nakamura, H. (1992). Midwinter Suppression of Baroclinic Wave Activity in the Pacific.
708 *Journal of Atmospheric Sciences*, 49(17), 1629–1642. <https://doi.org/10.1175/1520->
709 0469(1992)049<1629:MSOBWA>2.0.CO;2
- 710 Panetta, R. L. (1993). Zonal Jets in Wide Baroclinically Unstable Regions: Persistence and Scale
711 Selection. *Journal of the Atmospheric Sciences*, 50(14), 2073–2106.
712 [https://doi.org/10.1175/1520-0469\(1993\)050<2073:ZJIWBU>2.0.CO;2](https://doi.org/10.1175/1520-0469(1993)050<2073:ZJIWBU>2.0.CO;2)
- 713 Petoukhov, V., Rahmstorf, S., Petri, S., & Schellnhuber, H. J. (2013). Quasiresonant
714 amplification of planetary waves and recent Northern Hemisphere weather extremes.
715 *Proceedings of the National Academy of Sciences of the United States of America*, 110(14),
716 5336–5341. <https://doi.org/10.1073/pnas.1222000110>
- 717 Ropelewski, C. F., & Halpert, M. S. (1989). Precipitation Patterns Associated with the High
718 Index Phase of the Southern Oscillation. *Journal of Climate*, 2(3), 268–284.

- 719 [https://doi.org/10.1175/1520-0442\(1989\)002<0268:PPAWTH>2.0.CO;2](https://doi.org/10.1175/1520-0442(1989)002<0268:PPAWTH>2.0.CO;2)
- 720 Ryoo, J. M., Kaspi, Y., Waugh, D. W., Kiladis, G. N., Waliser, D. E., Fetzer, E. J., & Kim, J.
721 (2013). Impact of rossby wave breaking on U.S. west coast winter precipitation during
722 ENSO events. *Journal of Climate*, 26(17), 6360–6382. [https://doi.org/10.1175/JCLI-D-12-](https://doi.org/10.1175/JCLI-D-12-00297.1)
723 00297.1
- 724 Sampe, T., Nakamura, H., Goto, A., & Ohfuchi, W. (2010). Significance of a midlatitude SST
725 frontal zone in the formation of a storm track and an eddy-driven westerly jet. *Journal of*
726 *Climate*, 23(7), 1793–1814. <https://doi.org/10.1175/2009JCLI3163.1>
- 727 Schneider, E. K. (1977). Axially Symmetric Steady-State Models of the Basic State for
728 Instability and Climate Studies. Part II. Nonlinear Calculations. *Journal of the Atmospheric*
729 *Sciences*, 34(2), 280–296. [https://doi.org/10.1175/1520-](https://doi.org/10.1175/1520-0469(1977)034<0280:ASSSMO>2.0.CO;2)
730 0469(1977)034<0280:ASSSMO>2.0.CO;2
- 731 Seager, R., Murtugudde, R., Naik, N., Clement, A., Gordon, N., & Miller, J. (2003). Air-sea
732 interaction and the seasonal cycle of the subtropical anticyclones. *Journal of Climate*,
733 16(12), 1948–1966. [https://doi.org/10.1175/1520-0442\(2003\)016<1948:AIATSC>2.0.CO;2](https://doi.org/10.1175/1520-0442(2003)016<1948:AIATSC>2.0.CO;2)
- 734 Smith, S. R., Green, P. M., Leonardi, A. P., & O'Brien, J. J. (1998). Role of Multiple-Level
735 Tropospheric Circulations in Forcing ENSO Winter Precipitation Anomalies. *Monthly*
736 *Weather Review*, 126(12), 3102–3116. [https://doi.org/10.1175/1520-](https://doi.org/10.1175/1520-0493(1998)126<3102:ROMLTC>2.0.CO;2)
737 0493(1998)126<3102:ROMLTC>2.0.CO;2
- 738 Solomon, A., Polvani, L. M., Waugh, D. W., & Davis, S. M. (2016). Contrasting upper and
739 lower atmospheric metrics of tropical expansion in the Southern Hemisphere. *Geophysical*
740 *Research Letters*, 43(19), 10,496–10,503. <https://doi.org/10.1002/2016GL070917>
- 741 Son, S. W., & Lee, S. (2005). The response of westerly jets to thermal driving in a primitive

- 742 equation model. *Journal of the Atmospheric Sciences*, 62(10), 3741–3757.
743 <https://doi.org/10.1175/JAS3571.1>
- 744 Strong, C., & Davis, R. E. (2008). Variability in the position and strength of winter jet stream
745 cores related to northern hemisphere teleconnections. *Journal of Climate*, 21(3), 584–592.
746 <https://doi.org/10.1175/2007JCLI1723.1>
- 747 Wallace, J. M., & Gutzler, D. S. (1981). Teleconnections in the Geopotential Height Field during
748 the Northern Hemisphere Winter. *Monthly Weather Review*, 109(4), 784–812.
749 [https://doi.org/10.1175/1520-0493\(1981\)109<0784:TITGHF>2.0.CO;2](https://doi.org/10.1175/1520-0493(1981)109<0784:TITGHF>2.0.CO;2)
- 750 Waugh, D. W., Grise, K. M., Seviour, W. J. M., Davis, S. M., Davis, N., Adam, O., ... Ming, A.
751 (2018). Revisiting the relationship among metrics of tropical expansion. *Journal of Climate*,
752 31(18), 7565–7581. <https://doi.org/10.1175/JCLI-D-18-0108.1>
- 753 Winters, A. C., & Martin, J. E. (2016). Synoptic and mesoscale processes supporting vertical
754 superposition of the polar and subtropical jets in two contrasting cases. *Quarterly Journal of*
755 *the Royal Meteorological Society*, 142(695), 1133–1149. <https://doi.org/10.1002/qj.2718>
- 756 Woollings, T., Barriopedro, D., Methven, J., Son, S. W., Martius, O., Harvey, B., ... Seneviratne,
757 S. (2018). Blocking and its Response to Climate Change. *Current Climate Change Reports*,
758 4(3), 287–300. <https://doi.org/10.1007/s40641-018-0108-z>
- 759 Woollings, T., Czuchnicki, C., & Franzke, C. (2014). Twentieth century North Atlantic jet
760 variability. *Quarterly Journal of the Royal Meteorological Society*, 140(680), 783–791.
761 <https://doi.org/10.1002/qj.2197>
- 762 Yu, B., & Lin, H. (2019). Modification of the wintertime Pacific–North American pattern related
763 North American climate anomalies by the Asian–Bering–North American teleconnection.
764 *Climate Dynamics*, 53(1–2), 313–328. <https://doi.org/10.1007/s00382-018-4586-4>

- 765 Yuval, J., & Kaspi, Y. (2018). Eddy sensitivity to jet characteristics. *Journal of the Atmospheric*
766 *Sciences*, 75(5), 1371–1383. <https://doi.org/10.1175/JAS-D-17-0139.1>
- 767 Zhang, W., & Villarini, G. (2018). Uncovering the role of the East Asian jet stream and
768 heterogeneities in atmospheric rivers affecting the western United States. *Proceedings of the*
769 *National Academy of Sciences of the United States of America*, 115(5), 891–896.
770 <https://doi.org/10.1073/pnas.1717883115>
771